


Multistage electronic nematic transitions in cuprate superconductors: A functional-renormalization-group analysis

Masahisa Tsuchiizu,^{1,2} Kouki Kawaguchi,² Youichi Yamakawa,² and Hiroshi Kontani²

¹*Department of Physics, Nara Women's University, Nara 630-8506, Japan*

²*Department of Physics, Nagoya University, Nagoya 464-8602, Japan*

 (Received 15 May 2017; revised manuscript received 17 December 2017; published 19 April 2018)

Recently, complex rotational symmetry-breaking phenomena have been discovered experimentally in cuprate superconductors. To find the realized order parameters, we study various unconventional charge susceptibilities in an unbiased way by applying the functional-renormalization-group method to the d - p Hubbard model. Without assuming the wave vector of the order parameter, we reveal that the most dominant instability is the uniform ($\mathbf{q} = \mathbf{0}$) charge modulation on the p_x and p_y orbitals, which possesses d symmetry. This uniform nematic order triggers another nematic p -orbital density wave along the axial (Cu-Cu) direction at $\mathbf{Q}_a \approx (\pi/2, 0)$. It is predicted that uniform nematic order is driven by the spin fluctuations in the pseudogap region, and another nematic density-wave order at $\mathbf{q} = \mathbf{Q}_a$ is triggered by the uniform order. The predicted multistage nematic transitions are caused by Aslamazov–Larkin-type fluctuation-exchange processes.

DOI: [10.1103/PhysRevB.97.165131](https://doi.org/10.1103/PhysRevB.97.165131)

I. INTRODUCTION

In the normal state of high- T_c cuprate superconductors, interesting unconventional order parameters emerge due to the strong interference between the spin, charge, and orbital degrees of freedom. These phenomena should be directly related to the fundamental electronic states in the pseudogap region. The emergence of the charge-density-wave (CDW) states inside the pseudogap region has been confirmed by the x-ray and scanning tunneling microscopy measurements [1–6], as schematically shown in Fig. 1(a). The observed CDW pattern is shown in Fig. 1(b), in which the density modulations mainly occur on the oxygen p_x and p_y orbitals with antiphase (d -symmetry) form factor. The discovery of the CDW has promoted significant progress in the theoretical studies, such as the spin-fluctuation-driven density-wave scenarios [7–14] and the superconducting-fluctuation scenarios [15–18].

The origin and nature of the pseudogap phase below T^* remain unsolved. For example, it is unclear whether the pseudogap is a distinct phase or a continuous crossover. The short-range spin fluctuations at $T \sim T^*$ induce the large quasiparticle damping [19–21], which causes the pseudogap in the density of states. On the other hand, the phase transition around T^* has been reported by the resonant ultrasound spectroscopy [22], angle-resolved photoemission spectroscopy (ARPES) analysis [23], and magnetic torque measurement [24]. In particular, Ref. [24] discovered the C_4 symmetry-breaking (nematic) transition, and its natural candidate is the uniform CDW with d symmetry schematically shown in Fig. 1(c). A fundamental question, then, is what mechanism can account for such unconventional multistage CDW transitions? No CDW instabilities are given by the mean-field-level approximations, such as the random-phase approximation (RPA), unless large intersite interactions are introduced [13,25]. Therefore, higher-order many-body effects, called the vertex corrections (VCs), should be essential for the CDW formation [7–13,26].

In many spin-fluctuation-driven CDW scenarios, the CDW wave vector is given by the minor nesting vector \mathbf{Q}_a or \mathbf{Q}_d in Fig. 1(d); \mathbf{Q}_a is the “axial-wave vector” parallel to the nearest Cu-Cu direction, and \mathbf{Q}_d is the “diagonal-wave vector.” The experimental axial CDW is obtained if the Aslamazov–Larkin VCs (AL-VCs) are taken into account [13]. In addition, the uniform ($\mathbf{q} = \mathbf{0}$) CDW instability has been studied intensively based on the Hubbard models [9,27–30]. In these studies, however, it was difficult to exclude the possibility that the CDW susceptibility has the maximum at finite \mathbf{q} .

Theoretically, it is difficult to analyze the spin and charge susceptibilities with general wave vector \mathbf{q} on equal footing by including the VCs in an unbiased way. For this purpose, in principle, the functional-renormalization-group (fRG) method would be the best theoretical method. The pioneering fRG studies [9,28] were performed only in the weak-coupling region, so the obtained CDW instability is small and its \mathbf{q} dependence is not clear. To overcome this problem, we have to improve the numerical accuracy of the fRG method, and apply it to the two-dimensional Hubbard model in the strong-coupling region.

In this paper, we study the orbital-dependent spin and charge susceptibilities for various symmetries on equal footing by analyzing the higher-order VCs in an unbiased way using the improved fRG method. We find that the uniform CDW accompanied by the p -orbital polarization ($n_x \neq n_y$), shown in Fig. 1(c), is driven by the antiferro spin fluctuations. In this uniform nematic CDW phase, another nematic CDW instability emerges at the wave vector $\mathbf{q} = \mathbf{Q}_a$ as shown in Fig. 1(b). The present study indicates that the uniform p -orbital polarization appears in the pseudogap region, and the axial $\mathbf{q} = \mathbf{Q}_a$ CDW is induced at $T_{\text{CDW}} < T^*$. These multistage CDW transitions in under-doped cuprates originate from the higher-order AL-type VCs.

In the present study, we use the functional RG + constrained RPA (RG + cRPA) method. The advantage of this

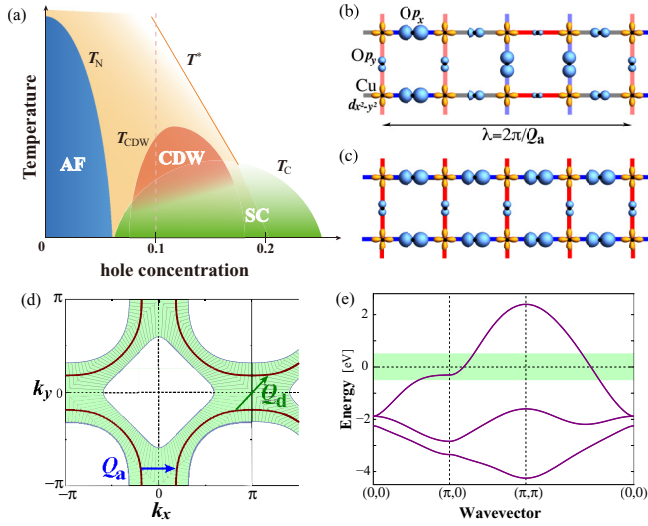


FIG. 1. (a) Schematic phase diagram of the high- T_c cuprate superconductors. T^* , T_{CDW} , T_N , and T_c are the transition temperatures for the pseudogap state, CDW order, magnetic order, and superconductivity, respectively. We study the 10%-doping case shown by the vertical broken line. (b) Schematic charge distribution in the d -symmetry p O-CDW state with the wave vector $\mathbf{q} = \mathbf{Q}_a \approx (0.5\pi, 0)$. (c) The uniform nematic p O-CDW state with $n_x \neq n_y$. (d) The Fermi surface and (e) energy dispersion of the present d - p model. The lower-energy region ($|E| < \Lambda_0 = 0.5$ eV) is divided into the $N_p = 128$ patches to perform the RG analysis.

method had been explained in Refs. [31–34] and Appendix A in detail.

II. MODEL AND THEORETICAL METHOD

Here, we study a standard three-orbital d - p Hubbard model [13,33,35] expressed as $H = \sum_{\mathbf{k},\sigma} \mathbf{c}_{\mathbf{k},\sigma}^\dagger \hat{h}_0(\mathbf{k}) \mathbf{c}_{\mathbf{k},\sigma} + U \sum_j n_{d,j,\uparrow} n_{d,j,\downarrow}$, where $\mathbf{c}_{\mathbf{k},\sigma}^\dagger = (d_{\mathbf{k},\sigma}^\dagger, p_{x,\mathbf{k},\sigma}^\dagger, p_{y,\mathbf{k},\sigma}^\dagger)$ is the creation operator for the electron on d , p_x , and p_y orbitals, and $\hat{h}_0(\mathbf{k})$ is the kinetic term given as the OMTO model in Refs. [35,36]. (The numerical results are unchanged if another realistic 1MTO model is used; see Appendix B.) U is the Hubbard-type on-site Coulomb interaction for the d orbital, and $n_{d,j,\sigma} = d_{j,\sigma}^\dagger d_{j,\sigma}$ at site \mathbf{j} . Hereafter, we study the 10%-hole-doping case. The Fermi surface (FS) and the band structure are shown in Figs. 1(d) and 1(e), respectively.

By using the RG + cRPA theory in Ref. [33], we find that the spin susceptibility for d electrons,

$$\chi^{\text{spin}}(\mathbf{q}) = \frac{1}{2} \int_0^{1/T} d\tau \langle S_d(\mathbf{q}, \tau) S_d(-\mathbf{q}, 0) \rangle, \quad (1)$$

and the B_{1g} -symmetry (d -symmetry) charge susceptibility for p electrons,

$$\chi_d^{p\text{-orb}}(\mathbf{q}) = \frac{1}{2} \int_0^{1/T} d\tau \langle n_d^{p\text{-orb}}(\mathbf{q}, \tau) n_d^{p\text{-orb}}(-\mathbf{q}, 0) \rangle, \quad (2)$$

are the most enhanced susceptibilities [33]. Here, $S_d(\mathbf{q}, \tau)$ is the d electron-spin operator, and $n_d^{p\text{-orb}}(\mathbf{q}) \equiv n_x(\mathbf{q}) - n_y(\mathbf{q})$ [$n_{x(y)}(\mathbf{q}) = \sum_{\mathbf{k},\sigma} p_{x(y),\mathbf{k},\sigma}^\dagger p_{x(y),\mathbf{k}+\mathbf{q},\sigma}$] is the p -orbital charge-density-wave (p O-CDW) operator with B_{1g} symmetry. If

$\chi_d^{p\text{-orb}}(\mathbf{q})$ diverges at $\mathbf{q} = \mathbf{Q}_a$ ($\mathbf{q} = \mathbf{0}$), the p O-CDW order shown in Fig. 1(b) [Fig. 1(c)], which is the CDW on p orbitals, is realized. We verified that the charge susceptibilities with non- B_{1g} symmetries, such as the A_{1g} -symmetry total charge susceptibility for $n \equiv n_d + n_x + n_y$, remain small even in the strong-coupling region [33].

In the RG + cRPA method, we calculate the scattering processes involving higher-energy states $|E_{\mathbf{k},v}| > \Lambda_0$ [v being the band index; see Fig. 1(e)] using the RPA with the energy-constraint and incorporate their contributions into the initial vertex functions of the RG equations [31–34]. Using the RPA, the higher-energy processes are calculated accurately by dropping the VCs, which are less important for higher-energy processes. The lower-energy scattering processes for $|E_{\mathbf{k},v}| < \Lambda_0$ are calculated by solving the RG equations, based on the N_p -patch RG scheme [27,37]. Hereafter, we put $N_p = 128$ and $\Lambda_0 = 0.5$ eV. In the RG + cRPA method, the numerical accuracy of the susceptibilities is greatly improved even in the weak-coupling region since the cRPA is used for the higher-energy processes, for which the N_p -patch RG scheme is less accurate. We verified that the numerical results are essentially independent of the choice of Λ_0 when $E_F \gtrsim \Lambda_0 \gg T$.

By solving the RG equations, many-body vertices are gradually renormalized as reducing the energy scale $\Lambda_l = \Lambda_0 e^{-l}$ with increasing l (≥ 0). In principle, the renormalization of the vertex saturates when Λ_l reaches $\sim T$ [37,38]. Here, we introduce the lower-energy cutoff $\Lambda_{\text{low}} (\sim T)$ in the RG equations for the four-point vertex $\Gamma_l^{s(c)}$, and stop the renormalization at $\Lambda_l = \Lambda_{\text{low}}$; see Appendix A and Ref. [9]. [We do not introduce the lower-energy cutoff in the RG equations for $\chi^{s,c}(\mathbf{q})$.] In the previous study [33], we set a large cutoff $\Lambda_{\text{low}} = \pi T$ to achieve stable numerical results. When $\Lambda_{\text{low}} \gg T$, the uniform ($\mathbf{q} = \mathbf{0}$) nematic susceptibility is especially underestimated compared with $\mathbf{q} \neq \mathbf{0}$ instabilities, as we discuss later. Since we have improved the numerical accuracy in solving the RG equations, we can use a smaller natural cutoff $\Lambda_{\text{low}} = T$. For this reason, we can obtain the \mathbf{q} dependence of the susceptibility accurately, including $\mathbf{q} \approx \mathbf{0}$.

We find that the numerical accuracy and stability are improved by employing the Wick-ordered scheme of the fRG formalism, in which the cutoff function $\Theta_{\leq}^{\Lambda}(\epsilon) = \Theta(\Lambda - |\epsilon|)$ is used for the Green's function [37]. In this scheme, in principle, the VCs due to the higher-energy processes are included more accurately compared with using another cutoff function $\Theta_{\geq}^{\Lambda}(\epsilon) = \Theta(|\epsilon| - \Lambda)$ based on the Kadanoff–Wilson scheme used in Ref. [33].

III. MULTISTAGE ELECTRONIC NEMATIC TRANSITIONS

In Figs. 2(a) and 2(b), we show the p O-CDW susceptibility $\chi_d^{p\text{-orb}}(\mathbf{q})$ given by the RG + cRPA method for $U = 4.32$ eV at $T = 0.1$ eV. The large peaks obtained at $\mathbf{q} = \mathbf{0}$, \mathbf{Q}_a , and \mathbf{Q}_d originate from the VCs, since the RPA result is less singular, as seen in Fig. 2(b). As shown in Figs. 2(a)–2(c), the most dominant peak locates at $\mathbf{q} = \mathbf{0}$. This is consistent with the experimental uniform nematic transition at T^* ($> T_{\text{CDW}}$) [24]. We also obtain the peak structures at $\mathbf{q} = \mathbf{Q}_a$ and \mathbf{Q}_d , consistently with our previous fRG study [33]. Figure 2(c) shows that $\chi_d^{p\text{-orb}}(\mathbf{0})$ monotonically increases with decreasing T ,

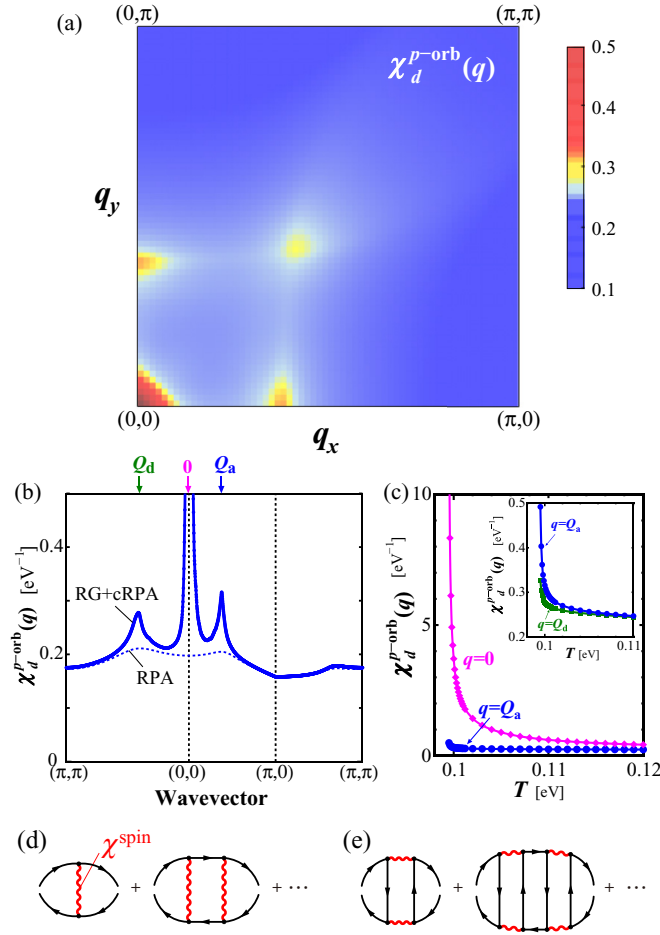


FIG. 2. (a), (b) The RG + cRPA result of the pO -CDW susceptibility $\chi_d^{p\text{-orb}}(\mathbf{q})$ obtained for $U = 4.32$ eV at $T = 0.1$ eV. The RPA result is also shown for comparison in panel (b). The axial wave vector is $\mathbf{Q}_a \approx (0.37\pi, 0)$ and the diagonal wave vector is $\mathbf{Q}_d \approx (0.40\pi, 0.40\pi)$. Both \mathbf{Q}_a and \mathbf{Q}_d correspond to the wave vector connecting the hot spots shown in Fig. 1(b). (c) T dependence of $\chi_d^{p\text{-orb}}(\mathbf{q})$ for $U = 4.32$ eV. (d) VCs due to MT processes. (e) VCs due to AL processes.

consistently with the recent electronic nematic susceptibility measurement [39]. At low temperatures, $\chi_d^{p\text{-orb}}(\mathbf{Q}_a)$ increases steeply and becomes larger than $\chi_d^{p\text{-orb}}(\mathbf{Q}_d)$, shown in the inset of Fig. 2(c). Note that the temperature $T = 0.1$ eV is comparable to $T^* \sim 300$ K if the mass-enhancement factor $m^*/m_{\text{band}} \sim 3$ is taken into account.

The enhancement of $\chi_d^{p\text{-orb}}(\mathbf{q})$ is caused by the spin fluctuations, due to the strong charge-spin interplay given by the VCs. The moderate peak at \mathbf{Q}_d is caused by the Maki-Thompson (MT)-VCs, given by the series of the single-fluctuation-exchange processes shown in Fig. 2(d) [11,12]. However, the MT-VCs cannot account for the dominant peaks at $\mathbf{q} = \mathbf{0}$ and \mathbf{Q}_a . Recently, it was found that the uniform nematic order in the Fe-based superconductors [26,40] and $\text{Sr}_3\text{Ru}_2\text{O}_7$ [31,41] is driven by the AL-VC, given by the series of the double-fluctuation-exchange processes shown in Fig. 2(e). In fact, the first term in Fig. 2(e) is proportional to $\sum_{\mathbf{k}} \chi^{\text{spin}}(\mathbf{k} + \mathbf{q}) \chi^{\text{spin}}(\mathbf{k})$, which takes a large value for $\mathbf{q} = \mathbf{0}$ when $\chi_{\text{max}}^{\text{spin}} \gg 1$ [26,42]. Later, we demonstrate that the AL-VC

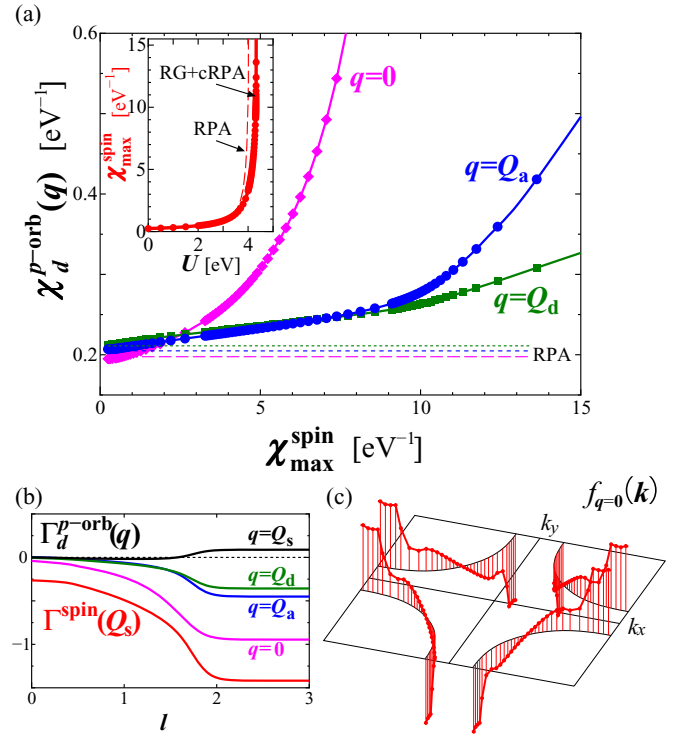


FIG. 3. (a) RG + cRPA result of $\chi_d^{p\text{-orb}}(\mathbf{q})$ at three peak positions as a function of $\chi_{\text{max}}^{\text{spin}} (\Delta E_p = 0)$. The RPA results are also shown by lines. In the inset, the U dependence of $\chi_{\text{max}}^{\text{spin}}$ is shown. (b) Scaling flows of the effective four-point vertices for the pO -CDW with d symmetry, for $U = 4.32$ eV at $T = 0.1$ eV. $l (\geq 0)$ is the scaling parameter. The scaling flows for spin channel are also shown where \mathbf{Q}_s is the nesting vector $\approx (\pi, 0.78\pi)$ or $(0.78\pi, \pi)$. (c) The optimized form factor $f_{q=0}(\mathbf{k})$ on the FS, which has d symmetry.

causes the uniform and axial CDW instabilities in the present d - p model.

Next, we investigate the U dependencies of the susceptibilities. In the inset of Fig. 3(a), we show the U dependence of $\chi_{\text{max}}^{\text{spin}} \equiv \max_{\mathbf{q}} \{\chi^{\text{spin}}(\mathbf{q})\}$. Thanks to the numerical accuracy of the RG + cRPA method, $\chi_{\text{max}}^{\text{spin}}$ perfectly follows the RPA result for the wide weak-coupling region ($U < 4$ eV). To clarify the close interplay between spin and orbital fluctuations, we plot the peak values of $\chi_d^{p\text{-orb}}(\mathbf{q})$ as a function of $\chi_{\text{max}}^{\text{spin}}$ in Fig. 3(a). In contrast to $\chi_{\text{max}}^{\text{spin}}$, $\chi_d^{p\text{-orb}}(\mathbf{q})$ strongly deviates from the RPA result, indicating the significance of the VCs. With increasing U , the peak position of $\chi_d^{p\text{-orb}}(\mathbf{q})$ shifts to $\mathbf{q} = \mathbf{0}$ at $\chi_{\text{max}}^{\text{spin}} \sim 2.5$, and $\chi_d^{p\text{-orb}}(\mathbf{0})$ exceeds the spin susceptibility for $\chi_{\text{max}}^{\text{spin}} \gtrsim 10$ eV $^{-1}$.

To understand the origin of the enhancement of $\chi_d^{p\text{-orb}}(\mathbf{q})$, we analyze the scaling flow of the effective interaction for the pO -CDW introduced as

$$\Gamma_d^{p\text{-orb}}(\mathbf{q}) \equiv \Gamma_{x;x}^c(\mathbf{q}) + \Gamma_{y;y}^c(\mathbf{q}) - \Gamma_{x;y}^c(\mathbf{q}) - \Gamma_{y;x}^c(\mathbf{q}),$$

with

$$\Gamma_{\alpha;\beta}^c(\mathbf{q}) \equiv \sum_{\mathbf{k}, \mathbf{k}'} \Gamma_l^c(\mathbf{k} + \mathbf{q}, \mathbf{k}; \mathbf{k}' + \mathbf{q}, \mathbf{k}') \times u_{\alpha}^*(\mathbf{k} + \mathbf{q}) u_{\alpha}(\mathbf{k}) u_{\beta}(\mathbf{k}' + \mathbf{q}) u_{\beta}^*(\mathbf{k}').$$

Here Γ_l^c is the charge-channel four-point vertex, which is a moderate function of the Fermi momenta in the parameter range of the present numerical study. $u_\alpha(\mathbf{k})$ is the matrix element connecting the p orbitals ($\alpha = x, y$) and the conduction band [33]. The scaling flow of $\Gamma_d^{p\text{-orb}}(\mathbf{q})$ is shown in Fig. 3(b), with the scaling parameter $l = \ln(\Lambda_0/\Lambda_l)$. The negative effective interaction drives the enhancement of the corresponding instability. We also plot the effective interaction for the spin channel, $\Gamma^{\text{spin}}(\mathbf{Q}_s)$. For the spin channel, $\Gamma^{\text{spin}}(\mathbf{Q}_s) \sim -U$ at $l = 0$, and it is renormalized like the RPA as $\Gamma_l^{\text{spin}} = \Gamma_0^{\text{spin}}/(1 - c|\Gamma_0^{\text{spin}}|l)$ for $l \lesssim \ln(\Lambda_0/T) = 1.6$, where c is the density of states. For the charge channel, although $\Gamma_d^{p\text{-orb}}(\mathbf{q})$ at $l = 0$ is quite small, it is strongly renormalized to be a large negative value. This result means that the CDW instability originates from the VC going beyond the RPA.

We also calculate the d -electron charge susceptibility with form factor $f_q(\mathbf{k})$, which is given as

$$\chi^{d\text{-orb}}(\mathbf{q}) = \frac{1}{2} \int_0^{1/T} d\tau \langle B(\mathbf{q}, \tau) B(-\mathbf{q}, 0) \rangle, \quad (3)$$

where $B(\mathbf{q}) = \sum_{k,\sigma} f_q(\mathbf{k}) d_{k-q/2,\sigma}^\dagger d_{k+q/2,\sigma}$. The numerically optimized $f_q(\mathbf{k})$ at $\mathbf{q} = \mathbf{0}$ is shown in Fig. 3(c), which has B_{1g} symmetry. Its Fourier transformation gives the modulation of the effective hopping integrals, called the $d_{x^2-y^2}$ -wave bond order. Since the \mathbf{k} dependence of $f_0(\mathbf{k})$ in Fig. 3(c) is similar to that of $|u_x(\mathbf{k})|^2 - |u_y(\mathbf{k})|^2$, the obtained $\chi_{\text{max}}^{\text{spin}}$ dependence of $\chi^{d\text{-orb}}(\mathbf{0})$ with the optimized form factor is similar to that of $\chi_d^{p\text{-orb}}(\mathbf{0})$ shown in Fig. 3(a). In Appendix C, we analyze the single- d -orbital Hubbard model, and find the strong enhancement of $\chi^{d\text{-orb}}(\mathbf{q})$ with the B_{1g} form factor at $\mathbf{q} = \mathbf{0}$, \mathbf{Q}_a , and \mathbf{Q}_d , very similarly to the p O-CDW susceptibilities shown in Figs. 2 and 3.

As shown in Fig. 2(c), $\chi_d^{p\text{-orb}}(\mathbf{0})$ increases divergently at $T \sim 0.1$ eV, and the uniform p -orbital polarization with $n_x \neq n_y$ depicted in Fig. 1(c) appears below the transition temperature. To discuss the CDW instabilities *inside* the nematic phase, we perform the RG + cRPA analysis in the presence of the uniform p O-CDW order $H' = -\frac{1}{2} \Delta E_p [n_x(\mathbf{0}) - n_y(\mathbf{0})]$. In Fig. 4(a), we plot the peak values of $\chi_d^{p\text{-orb}}(\mathbf{q})$ in the uniform p O-CDW state with $\Delta E_p = 0.3$ eV. Due to small $\Delta E_p > 0$, $\chi_d^{p\text{-orb}}(\mathbf{q})$ at $\mathbf{q} = \mathbf{Q}_a^x$ (along the x axis) strongly increases whereas that at $\mathbf{q} = \mathbf{Q}_a^y$ (along the y axis) decreases. Thus, the p O-CDW at $\mathbf{q} = \mathbf{Q}_a^x$ is expected to emerge below T_{CDW} , consistently with the phase diagram in Fig. 1(a).

IV. ORIGIN OF NEMATIC ORDERS

To confirm the mechanism of the nematic transition, we perform the diagrammatic calculation for the MT- and AL-VCs. These VCs can be obtained by solving the CDW equation introduced in Ref. [43] in the study of Fe-based superconductors. We analyze the linearized CDW equation introduced in Appendix D and in Ref. [44]. By solving the CDW equation, both MT- and AL-VCs shown in Figs. 2(d) and 2(e) with the optimized form factors are systematically generated. Figure 4(b) shows the eigenvalue of the linearized equation, λ_q , for $\Delta E_p = 0.1$ eV. Here, α_S is the spin Stoner factor, and the horizontal axis is proportional to $\chi_{\text{max}}^{\text{spin}}$. The CDW susceptibility increases

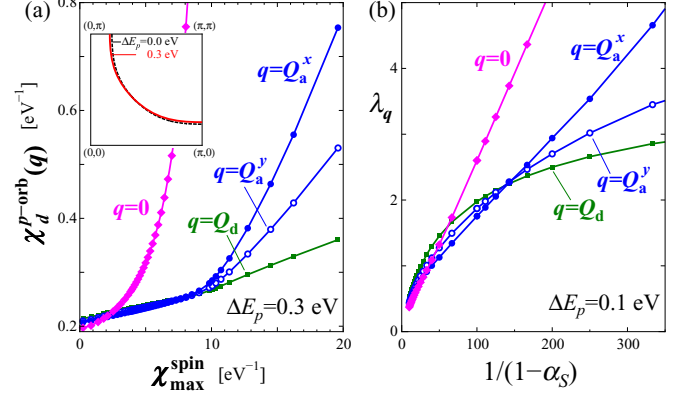


FIG. 4. (a) The RG + cRPA result of $\chi_d^{p\text{-orb}}(\mathbf{q})$ at $\mathbf{q} = \mathbf{0}$, $\mathbf{Q}_a^{x,y}$, and \mathbf{Q}_d as a function of $\chi_{\text{max}}^{\text{spin}}$ for $\Delta E_p = 0.3$ eV. The inset shows the FS. (b) The eigenvalues of the CDW susceptibility given by solving the linearized CDW equation in Appendix D for $\gamma = 0.3$ eV.

with the increase of λ_q . In Fig. 4(b), we set the quasiparticle damping $\gamma = 0.3$ eV. Note that λ_q decreases with γ , whereas its overall \mathbf{q} dependence is independent of γ , as shown in Appendix D. The obtained results are qualitatively consistent with the RG + cRPA results in Fig. 4(a). In Appendix D, we reveal that the CDW instabilities at $\mathbf{q} = \mathbf{0}$ and $\mathbf{q} = \mathbf{Q}_a$ are given by the higher-order AL-type VCs.

Finally, we explain why Λ_{low} should be set small. The RG equation for the $\mathbf{q} = \mathbf{0}$ vertex, $\bar{\Gamma}_l^c(\mathbf{k}; \mathbf{k}') \equiv \Gamma_l^c(\mathbf{k}, \mathbf{k}; \mathbf{k}', \mathbf{k}')$, is given as

$$d\bar{\Gamma}^c(\mathbf{k}; \mathbf{k}')/dl \propto \Lambda_l \dot{f}(\Lambda_l) \sum_{k''} \delta(|E_{k''}| - \Lambda_l) \bar{\Gamma}_l^c(\mathbf{k}; \mathbf{k}') \\ \times \bar{\Gamma}_l^c(\mathbf{k}''; \mathbf{k}') + \text{two other terms},$$

where $\dot{f}(\epsilon)$ is the derivative of the Fermi distribution function. Since the factor $|\dot{f}(\Lambda_l)|$ is small for $\Lambda_l \gtrsim 4T$, the obtained $\bar{\Gamma}_l^c$ is strongly reduced if $\Lambda_{\text{low}} \gg T$. In contrast, $\Gamma^{s,c}$ for $\mathbf{q} \neq \mathbf{0}$ is not so sensitive to Λ_{low} . For this reason, the renormalization effect of Γ_l^c is underestimated for $\mathbf{q} \approx \mathbf{0}$ if $\Lambda_{\text{low}} \gg T$. Then, the obtained $\chi_d^{p\text{-orb}}(\mathbf{0})$ is suppressed to be smaller than the peak values at $\mathbf{q} \neq \mathbf{0}$ if a large cutoff $\Lambda_{\text{low}} \gg T$ is used, similarly to the previous results for $\Lambda_{\text{low}} = \pi T$ [33]. In the present study, large $\chi_d^{p\text{-orb}}(\mathbf{0})$ is correctly obtained thanks to the use of the small cutoff $\Lambda_{\text{low}} = T$.

V. DOPING DEPENDENCE OF CHARGE-DENSITY-WAVE SUSCEPTIBILITIES

In the above sections, we studied the spin and charge susceptibilities in the d - p Hubbard model only for 10%-hole-doped case ($p = 0.10$). To understand the experimental phase diagram in Fig. 1(a), however, we have to study the doping dependence of susceptibilities. This issue is a very important but difficult goal for theorists. We find that the CDW is driven by the strong spin fluctuations, which strongly develop when the hole-density p approaches zero experimentally.

In the RG + cRPA theory, the CDW is driven by the strong spin fluctuations, and spin fluctuations develop as the hole carrier p approaches zero experimentally. For this

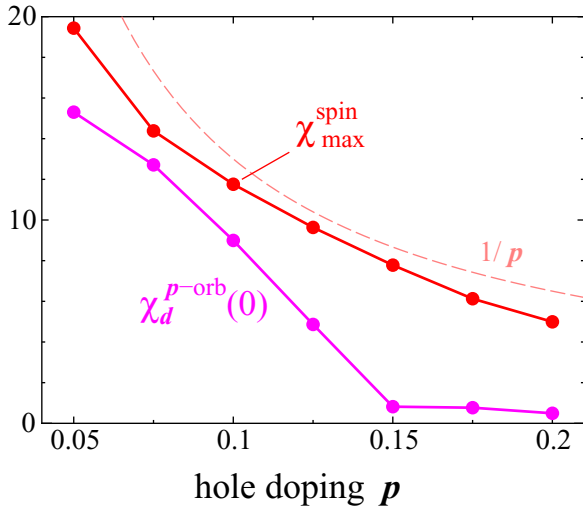


FIG. 5. Doping dependence of $\chi_d^{p\text{-orb}}(\mathbf{0})$ obtained by the RG + cRPA theory ($N_p = 64$) at $T = 0.1$ eV. The obtained $\chi_d^{p\text{-orb}}(\mathbf{0})$ linearly increases as p approaches unity, consistently with T^* in the experimental phase diagram in Fig. 1(a) in the main text. For $p \lesssim 0.1$, $\chi_d^{p\text{-orb}}(\mathbf{0})$ exceeds $\chi_{\max}^{\text{spin}}$ for $T \lesssim 0.1$ eV.

reason, as shown in Fig. 5, the uniform CDW susceptibility $\chi_d^{p\text{-orb}}(\mathbf{0})$ linearly increases as p decreases accompanied by the increment of $\chi_{\max}^{\text{spin}}$ for $p \sim 0$. This result is consistent with the experimental p dependence of T^* in Fig. 1(a) in the main text. In Fig. 5, we modify U slightly so that the experimental approximate relation $\chi_{\max}^{\text{spin}} \propto 1/p$ is satisfied, as performed in our previous study [13]. We put $U = 4.31, 4.25$, and 4.06 eV for $p = 0.05, 0.10$, and 0.20 , respectively.

In contrast to T^* , T_{CDW} decreases near the half filling for $p < 0.1$, as depicted in Fig. 1(a). This behavior is also understood qualitatively based on the spin-fluctuation-driven mechanism. In fact, the axial CDW wavelength Q_a is given by the nesting vector between the neighboring hot spots, and $|Q_a|$ increases as p approaches zero. The CDW instability driven by the Aslamazov–Larkin vertex correction, which is qualitatively proportional to $\sum_q \chi^s(\mathbf{q})\chi^s(\mathbf{q} + \mathbf{Q}_a)$, is suppressed if $|Q_a|$ is very large, as we explained in Ref. [13]. Therefore, the difference in the doping-dependencies of T^* and T_{CDW} is qualitatively understood. It is an important future issue to reproduce the experimental phase diagram in Fig. 1(a) more completely, which is one of the greatest goals in this field.

VI. SUMMARY

In summary, we studied various unconventional CDW instabilities in the d - p Hubbard model by using the RG + cRPA method and predicted the multistage CDW transitions in cuprate superconductors. Based on the proposed spin-fluctuation-driven CDW mechanism, the following understanding has been reached: The short-range spin fluctuations drive the uniform nematic CDW around T^* , and it triggers the axial $\mathbf{q} = \mathbf{Q}_a$ CDW at T_{CDW} successively. We also explained the doping dependence of T^* based on the RG + cRPA theory. These results naturally explain the phase diagram in Fig. 1(a), except for heavily under-doped region. Although the uniform

CDW order cannot simply explain the pseudogap formation, the large quasiparticle damping [19–21] due to the short-range spin-fluctuations may induce the pseudogap for $T \lesssim T^*$.

ACKNOWLEDGMENTS

We are grateful to Y. Matsuda, T. Hanaguri, T. Shibauchi, Y. Kasahara, Y. Gallais, W. Metzner, T. Enss, L. Classen, and S. Onari for fruitful discussions. This work was supported by Grant-in-Aid for Scientific Research from the Ministry of Education, Culture, Sports, Science, and Technology, Japan, and in part by Nara Women’s University Intramural Grant for Project Research.

APPENDIX A: RENORMALIZATION GROUP EQUATIONS FOR THE FOUR-POINT VERTEX

In the main text, we analyzed the d - p Hubbard model by using the RG + cRPA method [32]. This method is the combination of the fRG theory and the cRPA. The RG + cRPA method enables us to perform reliable numerical study in the unbiased way. In this method, we introduce the original cutoff energy Λ_0 in order to divide each band into the higher- and lower-energy regions: The higher-energy scattering processes are calculated by using the cRPA: The lower-energy scattering processes are analyzed by solving the RG equations, in which the initial vertices in the differential equation are given by the cRPA.

In the present model, the bare Coulomb interaction term on d electrons is given as

$$H_U = \frac{1}{4} \sum_i \sum_{\sigma\sigma'\rho\rho'} U^{0;\sigma\sigma'\rho\rho'} d_{i\sigma}^\dagger d_{i\sigma'}^\dagger d_{i\rho} d_{i\rho'}, \quad (\text{A1})$$

$$U^{0;\sigma\sigma'\rho\rho'} = \frac{1}{2} U^{0;s} \vec{\sigma}_{\sigma\sigma'} \cdot \vec{\sigma}_{\rho\rho'} + \frac{1}{2} U^{0;c} \delta_{\sigma\sigma'} \delta_{\rho\rho'}, \quad (\text{A2})$$

where $U^{0;c} = U$ and $U^{0;s} = -U$.

The antisymmetrized full four-point vertex $\Gamma(\mathbf{k} + \mathbf{q}, \mathbf{k}; \mathbf{k}' + \mathbf{q}, \mathbf{k}')$, which is the dressed vertex of the bare vertex \hat{U} in Eq. (A2) in the microscopic Fermi-liquid theory, is depicted in Fig. 6(a). Reflecting the SU(2) symmetry of the present model, Γ is uniquely decomposed into the spin-channel and charge-

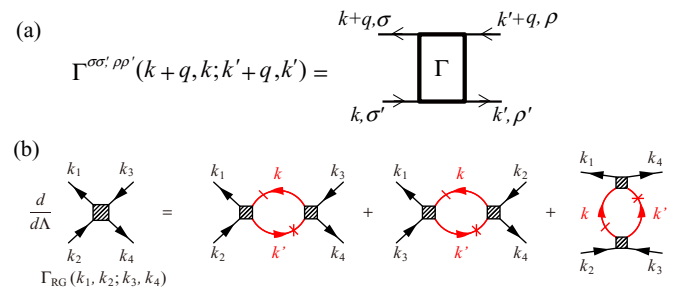


FIG. 6. (a) Definition of the full four-point vertex $\Gamma^{\sigma\sigma'\rho\rho'}(\mathbf{k} + \mathbf{q}, \mathbf{k}; \mathbf{k}' + \mathbf{q}, \mathbf{k}')$ in the microscopic Fermi-liquid theory. (b) The one-loop RG equation for the four-point vertex. The crossed lines represent the electron Green’s function with cutoff Λ . The slashed lines represent the electron propagations having energy shell Λ .

channel four-point vertices by using the following relation:

$$\begin{aligned} & \Gamma^{\sigma\sigma'\rho\rho'}(\mathbf{k} + \mathbf{q}, \mathbf{k}; \mathbf{k}' + \mathbf{q}, \mathbf{k}') \\ &= \frac{1}{2}\Gamma^s(\mathbf{k} + \mathbf{q}, \mathbf{k}; \mathbf{k}' + \mathbf{q}, \mathbf{k}')\vec{\sigma}_{\sigma\sigma'} \cdot \vec{\sigma}_{\rho'\rho} \\ &+ \frac{1}{2}\Gamma^c(\mathbf{k} + \mathbf{q}, \mathbf{k}; \mathbf{k}' + \mathbf{q}, \mathbf{k}')\delta_{\sigma,\sigma'}\delta_{\rho',\rho}, \end{aligned} \quad (\text{A3})$$

where $\sigma, \sigma', \rho, \rho'$ are spin indices, and $\vec{\sigma}$ is the Pauli matrix vector. We stress that $\Gamma^{c,s}$ are fully antisymmetrized, so the requirement by the Pauli principle is satisfied. We note that $\Gamma^{\uparrow\uparrow\uparrow\uparrow} = \frac{1}{2}\Gamma^c + \frac{1}{2}\Gamma^s$, $\Gamma^{\uparrow\uparrow\downarrow\downarrow} = \frac{1}{2}\Gamma^c - \frac{1}{2}\Gamma^s$, and $\Gamma^{\uparrow\downarrow\uparrow\downarrow} = \Gamma^s$.

In the RG formalism, the four-point vertex function is determined by solving the differential equations, called the RG equations. In the band-representation basis, the explicit form of the RG equations is given by [34]

$$\begin{aligned} & \frac{d}{d\Lambda}\Gamma_{\text{RG}}(k_1, k_2; k_3, k_4) \\ &= -\frac{T}{N}\sum_{k, k'}\left[\frac{d}{d\Lambda}G(k)G(k')\right] \\ &\times\left[\Gamma_{\text{RG}}(k_1, k_2; k, k')\Gamma_{\text{RG}}(k, k'; k_3, k_4)\right. \\ &- \Gamma_{\text{RG}}(k_1, k_3; k, k')\Gamma_{\text{RG}}(k, k'; k_2, k_4) \\ &\left.- \frac{1}{2}\Gamma_{\text{RG}}(k_1, k; k', k_4)\Gamma_{\text{RG}}(k, k_2; k_3, k')\right], \end{aligned} \quad (\text{A4})$$

where $G(k)$ is the Green's function multiplied by the Heaviside step function $\Theta(\Lambda - |E_{k,v}|)$, and k is the compact notation of the momentum, band, and spin indices: $k = (\mathbf{k}, \epsilon_n, \nu, \sigma)$. The diagrammatic representation of the RG equations is shown in Fig. 6(b). The first two contributions in the right-hand-side represent the particle-hole channels and the last contribution is the particle-particle channel.

In a conventional fRG method, Λ_0 is set larger than the bandwidth W_{band} , and the initial value is given by the bare Coulomb interaction in Eq. (A2). In the RG + cRPA method, we set $\Lambda_0 < W_{\text{band}}$, and the initial value is given by the constrained RPA to include the higher-energy processes without over counting of diagrams [32].

In the main text, we introduced the lower-energy cutoff $\Lambda_{\text{low}} (\sim T)$ in the RG equation for the four-point vertex: Eq. (A4). For this purpose, we multiply the cutoff function $[(\Lambda_{\text{low}}/\Lambda)^\zeta + 1]^{-1}$ to the right-hand side of Eq. (A4). Here, ζ is a parameter determining the width of this smooth cutoff, and we set $\zeta = 10$ in the main text. We do not introduce the lower-energy cutoff in the RG equation for the susceptibilities.

APPENDIX B: RG + cRPA ANALYSIS OF THE d - p MODEL WITH DIFFERENT HOPPING PARAMETERS

In Ref. [35], the authors derived the realistic d - p models for La-based cuprate by evaluating the hopping parameters on the basis of the N th-order muffin-tin orbitals (NMTO). The model parameters for $N = 0$ and $N = 1$ are given in Table I. The band structure of the $N = 0$ basis model (0MTO model) is very close to the local density approximation band structure near the Fermi energy. For this reason, we have analyzed the 0MTO model in the main text. On the other hand, the $N = 1$ basis model (1MTO model) appropriately reproduces

TABLE I. Hopping integrals for the $N = 0$ and $N = 1$ models given in Ref. [35]. The units are eV.

NMTO	$\epsilon_d - \epsilon_p$	t_{dd}	t_{pd}	t'_{pd}	t_{pp}	t'_{pp}	t''_{pp}	t'''_{pp}
$N = 0$	0.43	-0.10	0.96	-0.10	0.15	-0.24	0.02	0.11
$N = 1$	0.95	0.15	1.48	0.08	0.91	0.03	0.15	0.03

the overall oxygen bonding band structure with deep bottom energy $E \simeq -8$ eV. To check the reliability of our RG + cRPA results, we analyze the d - p model with the 1MTO model parameters.

Figure 7(a) shows the band structure of the 1MTO model. Here, we introduced the third-nearest d - d hopping $t_{dd}^{\text{3rd}} = -0.1$ eV to make the FS closer to Y-based cuprates. The FS of this model is shown in Fig. 7(b). Now, we analyze this model by using the RG + cRPA method. The parameters are the same as in the main text except for U . The number of patches is $N_p = 128$ and the initial cutoff is $\Lambda_0 = 0.5$ eV. The temperature is fixed at $T = 0.1$ eV.

In Fig. 7(c), we show the obtained $\chi_d^{p\text{-orb}}(\mathbf{q})$ for $U = 5.72$ eV. The RPA results are also shown for comparison. It has the largest peak at $\mathbf{q} = \mathbf{0}$ and the second largest peak at $\mathbf{q} = \mathbf{Q}_a$, respectively. The obtained \mathbf{q} dependence of $\chi_d^{p\text{-orb}}(\mathbf{q})$ is similar to Fig. 2(b). We also investigate the U dependencies of the spin and charge susceptibilities. As shown in the inset of Fig. 7(d), relatively large U is required for the enhancement of $\chi_{\text{max}}^{\text{spin}}$ in the 1MTO model, since the density of states of the d orbital at the Fermi energy in the 1MTO model is smaller than that in the 0MTO model [35]. In Fig. 7(d), we plot the peak values of $\chi_d^{p\text{-orb}}(\mathbf{q})$ as functions of $\chi_{\text{max}}^{\text{spin}}$. The obtained results are quite similar to Fig. 3(a) in the main text. Thus the spin-fluctuation-driven CDW instabilities are universal phenomena in both the 0MTO and 1MTO models.

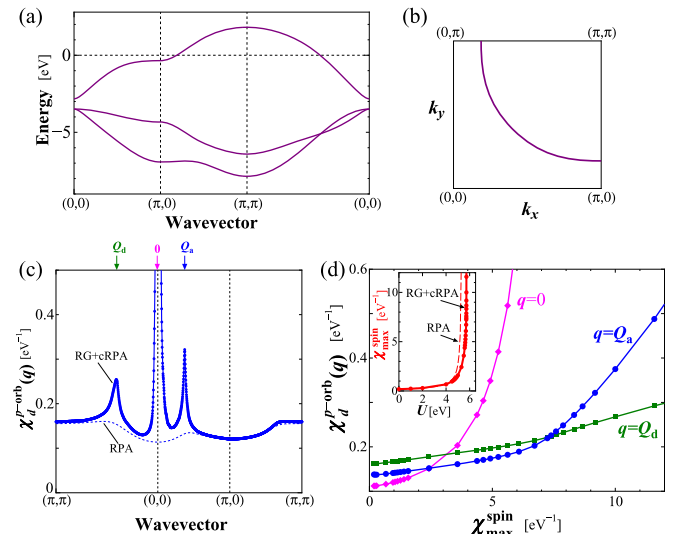


FIG. 7. (a) Energy dispersion and (b) FS of the d - p model with 1MTO model parameters. (c) RG + cRPA and RPA results for the p O-CDW susceptibility $\chi_d^{p\text{-orb}}(\mathbf{q})$ with $U = 5.72$ eV. (d) RG + cRPA result of $\chi_d^{p\text{-orb}}(\mathbf{q})$ at three peak positions as a function of $\chi_{\text{max}}^{\text{spin}}$.

In summary, we investigate the d - p model with 1MTO model parameters. We found that the results are very similar to those for the 0MTO model given in the main text. Therefore, the mechanism of the spin-fluctuation-driven CDW instabilities revealed in the main text is universal, independently of the details of the model parameters.

APPENDIX C: RG + cRPA ANALYSIS FOR SINGLE- d -ORBITAL HUBBARD MODEL

In the main text, we studied the 0MTO d - p Hubbard model based on the RG + cRPA theory and found that the p O-CDW susceptibilities develop strongly in the strong-spin-fluctuation region. Similar results are obtained in the 1MTO model in which $\epsilon_d - \epsilon_p$ is 0.53 eV larger than that in the 0MTO model, as we show in Appendix B. In these d - p models, any Coulomb interactions on p orbitals are not taken into account. Therefore, spin-fluctuation-driven CDW formation is also expected to be realized in the single- d -orbital Hubbard model with on-site Coulomb interaction.

Here, we study the single- d -orbital Hubbard model with the first-, the second-, and the third-nearest hopping integrals as $t = -0.50$ eV, $t' = 0.083$ eV, and $t'' = -0.10$ eV, respectively. The band structure and Fermi surface for $n = 0.90$ are shown in Figs. 8(a) and 8(b), respectively. We calculate the d -electron charge susceptibility $\chi^{d\text{-orb}}(\mathbf{q})$ with the B_{1g} form factor $f_q(\mathbf{k}) = \cos(k_x) - \cos(k_y)$ introduced in Eq. (3) in the main text. The results obtained are summarized in Fig. 8(c): Both $\chi^{d\text{-orb}}(\mathbf{0})$ and $\chi^{d\text{-orb}}(\mathbf{Q}_a)$ are strongly enlarged in the strong spin-fluctuation region, very similarly to the p O-CDW susceptibility shown in Fig. 3(a) in the main text.

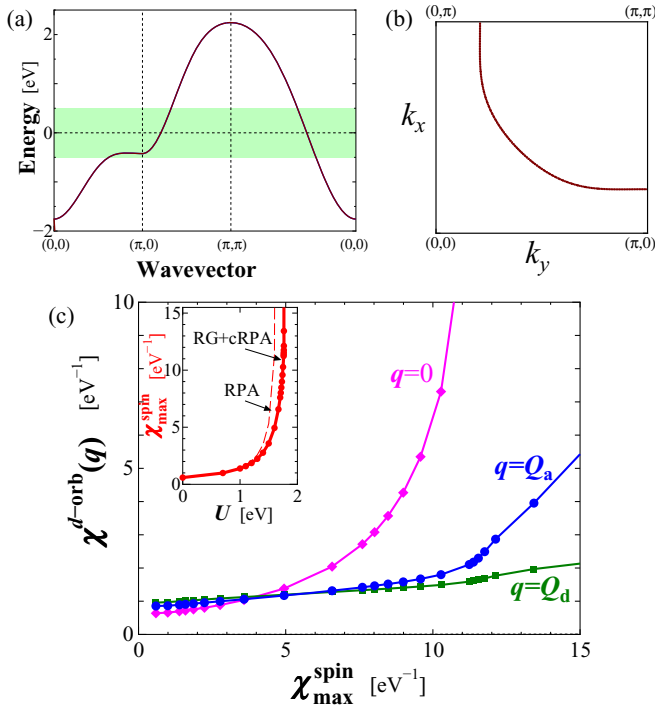


FIG. 8. (a) Energy dispersion and (b) FS of the single- d -orbital Hubbard model. (c) RG + cRPA result of the d -electron charge susceptibility with B_{1g} form factor $f_q(\mathbf{k}) = \cos(k_x) - \cos(k_y)$, $\chi_d^{d\text{-orb}}(\mathbf{q})$, as a function of $\chi_{\max}^{\text{spin}}$.

Therefore, it was verified that our main numerical results in the main text are unchanged even in the single- d -orbital model once the B_{1g} form factor is taken into account. We also analyzed the CDW equation for the single- d -orbital model, and obtained the strong CDW instability. The obtained form factor $\Delta\Sigma_0(\mathbf{k})$ has B_{1g} symmetry. In real space, this is the bond order (=modulation of hopping integrals) given by the Fourier transformation of the symmetry-breaking self-energy $\Delta\Sigma_0(\mathbf{k})$. Thus, the robustness of the spin-fluctuation-driven CDW mechanism has been clearly confirmed.

APPENDIX D: ANALYSIS OF LINEARIZED CHARGE-DENSITY-WAVE EQUATION

In the main text, we analyzed the d - p Hubbard model for cuprate superconductors in an unbiased manner by using the RG + cRPA method. We find that the nematic CDW with d form factor is the leading instability. The axial nematic CDW instability at $\mathbf{q} = \mathbf{Q}_a$ is the second strongest, and its strength increases under the static uniform CDW order. This result leads to the prediction that uniform nematic CDW occurs at the pseudogap temperature T^* , and the axial CDW at wave vector $\mathbf{q} = \mathbf{Q}_a$ is induced under T^* .

In this section, we study the CDW formation mechanism in cuprate superconductors based on the diagrammatic method to find which many-body processes cause the CDW order. Theoretically, the CDW order is given as the symmetry breaking in the self-energy $\Delta\Sigma(k)$. According to Refs. [26,44], the self-consistent CDW equation is

$$\Delta\Sigma(k) = (1 - P_{A_{1g}})T \sum_q V(q)G(k+q), \quad (\text{D1})$$

where $P_{A_{1g}}$ is the A_{1g} -symmetry projection operator, and $G(k) = [G_0^{-1}(k) - \Delta\Sigma(k)]^{-1}$ is the d -electron Green's function with the symmetry-breaking term $\Delta\Sigma$. $V(q) = U^2[\frac{3}{2}\chi^s(q) + \frac{1}{2}\chi^c(q) - \chi^0(q)] + U$, where $\chi^{s(c)}(q) = \chi^0(q)/[1 - (+)U\chi^0(q)]$ and $\chi^0(q) = -T \sum_k G(k+q)G(k)$.

To analyze the CDW state with arbitrary wave vector \mathbf{q} , we linearize Eq. (D1) with respect to $\Delta\Sigma$:

$$\lambda_q \Delta\Sigma_q(k) = T \sum_{k'} K(\mathbf{q}; k, k') \Delta\Sigma_q(k'), \quad (\text{D2})$$

where λ_q is the eigenvalue for the CDW for the wave vector \mathbf{q} . The CDW with wave vector \mathbf{q} appears when $\lambda_q = 1$, and the eigenvector $\Delta\Sigma_q(k)$ gives the CDW form factor. The kernel $K(\mathbf{q}, k, k')$ is given in Fig. 9(a), and its analytic expression is [44]

$$\begin{aligned} K(\mathbf{q}; k, k') &= \left(\frac{3}{2} V_0^s(k-k') + \frac{1}{2} V_0^c(k-k') \right) \\ &\times G_0(k'+\mathbf{q}/2)G_0(k'-\mathbf{q}/2) \\ &- T \sum_p \left(\frac{3}{2} V_0^s(p+\mathbf{q}/2)V_0^s(p-\mathbf{q}/2) \right. \\ &\left. + \frac{1}{2} V_0^c(p+\mathbf{q}/2)V_0^c(p-\mathbf{q}/2) \right) \\ &\times G_0(k-p)[\Lambda_q(k'; p) + \Lambda_q(k'; -p)], \quad (\text{D3}) \end{aligned}$$

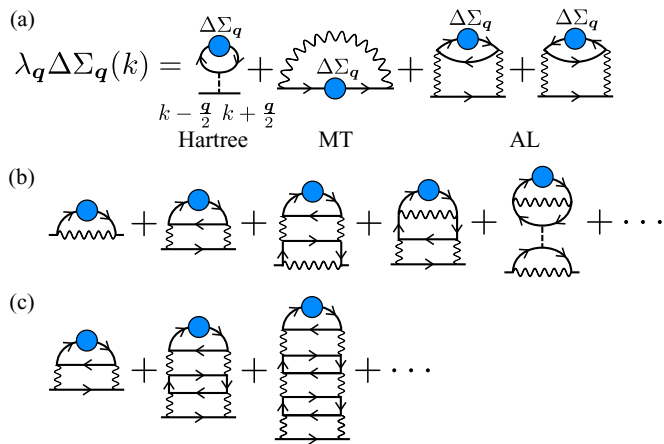


FIG. 9. (a) Schematic linearized CDW equation for general wave vector q . (b) Examples of the VCs generated by solving the linearized CDW equation. (c) Higher-order AL processes.

where $V_0^s(q) = U + U^2 \chi_0^s(q)$, $V_0^c(q) = -U + U^2 \chi_0^c(q)$, and $\Delta_q(k; p) \equiv G_0(k + \frac{q}{2})G_0(k - \frac{q}{2})G_0(k - p)$. The subscript 0 in Eq. (D3) represents the functions with $\Delta \Sigma = 0$.

By solving the linearized CDW equation (D2), many higher-order vertex corrections (VCs) are systematically generated. Some examples of the generated VCs are shown in Fig. 9(b). If we drop the Hartree term and MT term in $K(q; k, k')$, we obtain the series of higher-order AL-VCs shown in Fig. 9(c). The AL terms drive the $q = 0$ CDW instability since its functional form $\propto \sum_k \chi^s(k + q) \chi^s(k)$ is large for $q \approx 0$ [43].

Figure 10(a) shows the obtained q dependence of λ_q for $\alpha_S = 0.995$ at $T = 50$ meV. Here, we introduced the quasiparticle damping $\gamma = 0.3$ eV into $G_0(k)$. Here, λ_q is the largest at $q = 0$, and the second largest maximum is at $q = Q_a$. $\alpha_S \equiv U \max_q \{\chi_0^s(q)\}$ is the spin Stoner factor. We also show the eigenvalue λ_q^{AL} (and the second-largest eigenvalue $\lambda_q^{\text{AL,2nd}}$), which is obtained by dropping the Hartree and MT terms in the kernel. That is, λ_q^{AL} is given by the higher-order AL processes shown in Fig. 9(c). At $q = 0$ and Q_a , λ_q^{AL} is almost equal to the true eigenvalue λ_q .

In the present analysis, we dropped the ϵ_n dependence of $\Delta \Sigma_q(k)$ by performing the analytic continuation ($i\epsilon_n \rightarrow \epsilon$) and putting $\epsilon = 0$. We also dropped the ϵ_n dependence of the quasiparticle damping γ . Due to these simplifications, the obtained λ_q is overestimated. Therefore, we do not put the constraint $\lambda_q < 1$ here.

In Fig. 10(b), we show the eigenvalue λ_q^{MT} , which is obtained by dropping the Hartree and AL terms in the kernel. It is much smaller than λ_q at $q = 0$ and Q_a , whereas λ_q at $q = Q_d$ is comparable to the true eigenvalue. Therefore, the origin of the CDW instability at $q = 0$ and Q_a is the AL process, whereas that at $q = Q_d$ is mainly the MT process.

Figure 10(c) shows the eigenvalues at $q = 0$, Q_a , and Q_d as a function of α_S . As the spin susceptibility increases ($\alpha_S \gtrsim 0.98$), λ_q is drastically enlarged by the VCs, and $\lambda_{q=0}$ becomes the largest due to the AL processes. The form factor at $q = 0$, $\Delta \Sigma_0(k)$, has the d -wave symmetry, as shown in Fig. 10(d).

We stress that the eigenvalue λ_q is quickly suppressed by increasing γ , which is actually large in cuprates. Figures 10(e)

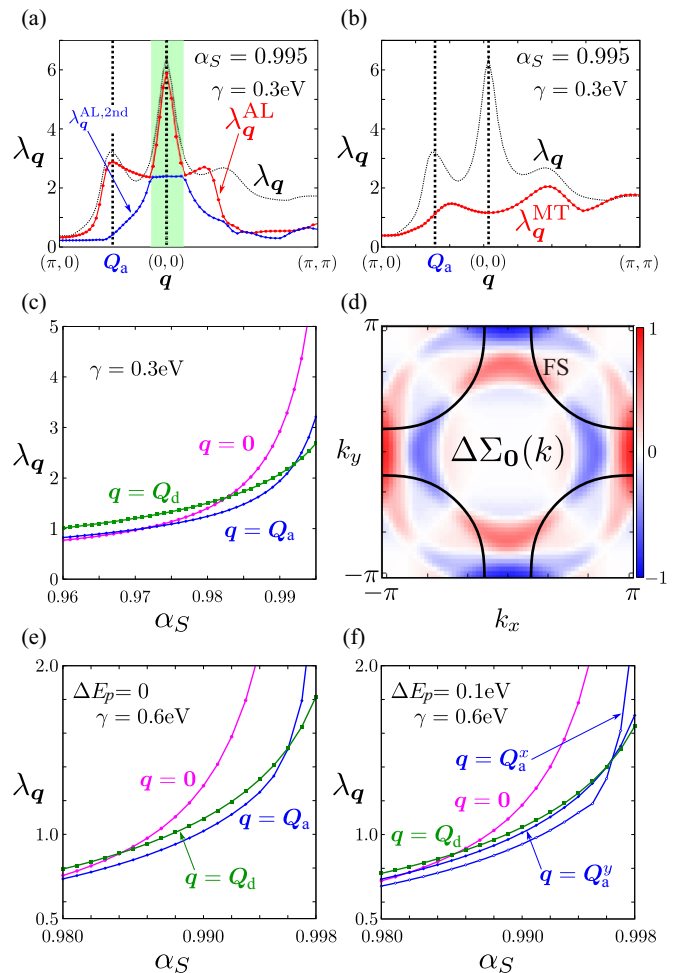


FIG. 10. (a), (b) q dependencies of λ_q , λ_q^{AL} , $\lambda_q^{\text{AL,2nd}}$, and λ_q^{MT} for $\alpha_S = 0.995$ and $\gamma = 0.3$ eV. (c) λ_q at $q = 0$, Q_a , and Q_d as a function of α_S for $\gamma = 0.3$ eV. (d) Form factor for $q = 0$ (d wave). (e), (f) λ_q as a function of α_S for $\gamma = 0.6$ eV in the cases of $\Delta E_p = 0$ and $\Delta E_p = 0.1$ eV, respectively.

and 10(f) show the CDW susceptibilities for the larger damping rate $\gamma = 0.6$ eV in the cases of $\Delta E_p = 0$ and $\Delta E_p = 0.1$ eV, respectively. (Note that the damping rate is renormalized to be $\sim \gamma/5$ in cuprates.) In Fig. 10(e), λ_q reaches unity first at $q = 0$ with increasing α_S . In the nematic state with $\Delta E_p = 0.1$ eV shown in Fig. 10(f), λ_q at $q = Q_a^x$ exceeds λ_{Q_d} for $\alpha_S > 0.996$. The corresponding eigenvalue is ~ 1.4 , which decreases with increasing γ . This result supports the main result of the present RG + cRPA study shown in Fig. 4(a) in the main text.

In summary, we analyzed the linearized CDW equation based on the d - p Hubbard model, by including both the MT and AL VCs into the kernel. When the spin fluctuations are strong ($\alpha_S \gtrsim 0.98$), the uniform nematic CDW has the strongest instability. The axial CDW instability is strongly magnified under the uniform CDW order, as we explain the main text. The results obtained are consistent with the results by the RG + cRPA in the main text. Thus, it is concluded that the higher-order AL processes give the CDW orders at $q = 0$ and Q_a .

- [1] G. Ghiringhelli, M. Le Tacon, M. Minola, S. Blanco-Canosa, C. Mazzoli, N. B. Brookes, G. M. De Luca, A. Frano, D. G. Hawthorn, F. He, T. Loew, M. M. Sala, D. C. Peets, M. Salluzzo, E. Schierle, R. Sutarto, G. A. Sawatzky, E. Weschke, B. Keimer, and L. Braicovich, *Science* **337**, 821 (2012).
- [2] J. Chang, E. Blackburn, A. T. Holmes, N. B. Christensen, J. Larsen, J. Mesot, R. Liang, D. A. Bonn, W. N. Hardy, A. Watenphul, M. von Zimmermann, E. M. Forgan, and S. M. Hayden, *Nat. Phys.* **8**, 871 (2012).
- [3] K. Fujita, M. H. Hamidian, S. D. Edkins, C. K. Kim, Y. Kohsaka, M. Azuma, M. Takano, H. Takagi, H. Eisaki, S. Uchida, A. Allais, M. J. Lawler, E. A. Kim, S. Sachdev, and J. C. Davis, *Proc. Natl. Acad. Sci. USA* **111**, E3026 (2014).
- [4] T. Wu, H. Mayaffre, S. Krämer, M. Horvatić, C. Berthier, W. N. Hardy, R. Liang, D. A. Bonn, and M.-H. Julien, *Nat. Commun.* **6**, 6438 (2015).
- [5] M. H. Hamidian, S. D. Edkins, C. K. Kim, J. C. Davis, A. P. Mackenzie, H. Eisaki, S. Uchida, M. J. Lawler, E. A. Kim, S. Sachdev, and K. Fujita, *Nat. Phys.* **12**, 150 (2015).
- [6] R. Comin and A. Damascelli, *Annu. Rev. Condens. Matter Phys.* **7**, 369 (2016).
- [7] J. C. Davis and D.-H. Lee, *Proc. Natl. Acad. Sci. USA* **110**, 17623 (2013).
- [8] M. A. Metlitski and S. Sachdev, *Phys. Rev. B* **82**, 075128 (2010).
- [9] C. Husemann and W. Metzner, *Phys. Rev. B* **86**, 085113 (2012).
- [10] K. B. Efetov, H. Meier, and C. Pépin, *Nat. Phys.* **9**, 442 (2013).
- [11] S. Sachdev and R. LaPlaca, *Phys. Rev. Lett.* **111**, 027202 (2013).
- [12] V. Mishra and M. R. Norman, *Phys. Rev. B* **92**, 060507 (2015).
- [13] Y. Yamakawa and H. Kontani, *Phys. Rev. Lett.* **114**, 257001 (2015).
- [14] P. P. Orth, B. Jeevanesan, R. M. Fernandes, and J. Schmalian, [arXiv:1703.02210](https://arxiv.org/abs/1703.02210).
- [15] E. Berg, E. Fradkin, S. A. Kivelson, and J. M. Tranquada, *New J. Phys.* **11**, 115004 (2009).
- [16] E. Fradkin, S. A. Kivelson, and J. M. Tranquada, *Rev. Mod. Phys.* **87**, 457 (2015).
- [17] Y. Wang, D. F. Agterberg, and A. V. Chubukov, *Phys. Rev. Lett.* **114**, 197001 (2015).
- [18] P. A. Lee, *Phys. Rev. X* **4**, 031017 (2014).
- [19] D. Senechal and A.-M. S. Tremblay, *Phys. Rev. Lett.* **92**, 126401 (2004).
- [20] B. Kyung, S. S. Kancharla, D. Senechal, A. -M. S. Tremblay, M. Civelli, and G. Kotliar, *Phys. Rev. B* **73**, 165114 (2006).
- [21] T. A. Maier, M. S. Jarrell, and D. J. Scalapino, *Physica C* **460–462**, 13 (2007).
- [22] A. Shekhter, B. J. Ramshaw, R. Liang, W. N. Hardy, D. A. Bonn, F. F. Balakirev, R. D. McDonald, J. B. Betts, S. C. Riggs, and A. Migliori, *Nature (London)* **498**, 75 (2013).
- [23] R.-H. He *et al.*, *Science* **331**, 1579 (2011).
- [24] Y. Sato, S. Kasahara, H. Murayama, Y. Kasahara, E.-G. Moon, T. Nishizaki, T. Loew, J. Porras, B. Keimer, T. Shibauchi, and Y. Matsuda, *Nat. Phys.* **13**, 1074 (2017).
- [25] S. Bulut, W. A. Atkinson, and A. P. Kampf, *Phys. Rev. B* **88**, 155132 (2013).
- [26] S. Onari and H. Kontani, *Phys. Rev. Lett.* **109**, 137001 (2012).
- [27] C. J. Halboth and W. Metzner, *Phys. Rev. Lett.* **85**, 5162 (2000).
- [28] C. Honerkamp, *Phys. Rev. B* **72**, 115103 (2005).
- [29] S.-Q. Su and T. A. Maier, *Phys. Rev. B* **84**, 220506(R) (2011).
- [30] M. Kitatani, N. Tsuji, and H. Aoki, *Phys. Rev. B* **95**, 075109 (2017).
- [31] M. Tsuchiizu, Y. Ohno, S. Onari, and H. Kontani, *Phys. Rev. Lett.* **111**, 057003 (2013).
- [32] M. Tsuchiizu, Y. Yamakawa, S. Onari, Y. Ohno, and H. Kontani, *Phys. Rev. B* **91**, 155103 (2015).
- [33] M. Tsuchiizu, Y. Yamakawa, and H. Kontani, *Phys. Rev. B* **93**, 155148 (2016).
- [34] R. Tazai, Y. Yamakawa, M. Tsuchiizu, and H. Kontani, *Phys. Rev. B* **94**, 115155 (2016).
- [35] P. Hansmann, N. Parragh, A. Toschi, G. Sangiovanni, and K. Held, *New J. Phys.* **16**, 033009 (2014).
- [36] In this paper, we used the hopping parameters of the 0MTO model in Ref. [35]. We verified that the numerical results are unchanged if we use another set of hopping parameters of the 1MTO model in Ref. [35]. The RG + cRPA results of the 1MTO model are shown in Appendix B.
- [37] W. Metzner, M. Salmhofer, C. Honerkamp, V. Meden, and K. Schönhammer, *Rev. Mod. Phys.* **84**, 299 (2012).
- [38] C. Bourbonnais, B. Guay, and R. Wortis, in *Theoretical Methods for Strongly Correlated Electrons*, edited by D. Sénéchal, A.-M. Tremblay, and C. Bourbonnais (Springer, New York, 2004), pp. 77–137.
- [39] Y. Mizukami, T. Shibauchi *et al.* (private communication).
- [40] H. Kontani and Y. Yamakawa, *Phys. Rev. Lett.* **113**, 047001 (2014).
- [41] Y. Ohno, M. Tsuchiizu, S. Onari, and H. Kontani, *J. Phys. Soc. Jpn.* **82**, 013707 (2013).
- [42] S. Caprara, C. Di Castro, M. Grilli, and D. Suppa, *Phys. Rev. Lett.* **95**, 117004 (2005).
- [43] S. Onari, Y. Yamakawa, and H. Kontani, *Phys. Rev. Lett.* **116**, 227001 (2016).
- [44] K. Kawaguchi, M. Tsuchiizu, Y. Yamakawa, and H. Kontani, *J. Phys. Soc. Jpn.* **86**, 063707 (2017).